INSTITUTE OF PHYSICS PUBLISHING JOURNAL OF PHYSICS D: APPLIED PHYSICS

J. Phys. D: Appl. Phys. **39** (2006) 700–711 doi:10.1088/0022-3727/39/4/016

Experimental and modelling investigations of a dielectric barrier discharge in low-pressure argon

E Wagenaars[1], R Brandenburg[2], W J M Brok[1], M D Bowden[3] and H-E Wagner[4]

[1] Department of Applied Physics, Eindhoven University of Technology, PO Box 513, 5600 MB Eindhoven, The Netherlands
[2] Institute of Low Temperature Plasma Physics e.V. (INP), F.-L.-Jahnstrasse 19, 17489 Greifswald, Germany
[3] Department of Physics and Astronomy, The Open University, Milton Keynes, MK7 6AA, UK
[4] Institute of Physics, Ernst-Moritz-Arndt University of Greifswald, Domstrasse 10a, 17489 Greifswald, Germany

E-mail: e.wagenaars@tue.nl and wagner@physik.uni-greifswald.de

Received 26 September 2005, in final form 9 December 2005
Published 3 February 2006
Online at stacks.iop.org/JPhysD/39/700

Abstract

The discharge behaviour of a dielectric barrier discharge (DBD) in low-pressure argon gas was investigated by experiments and modelling. The electrical characteristics and light emission dynamics of the discharge were measured and compared with the results of a two-dimensional fluid model. Our investigations showed that the discharge consisted of a single, diffuse discharge per voltage half-cycle. The breakdown phase of the low-pressure DBD (LPDBD) was investigated to be similar to the ignition phase of a low-pressure glow discharge without dielectrics, described by Townsend breakdown theory. The stable discharge phase of the LPDBD also showed a plasma structure with features similar to those of a classical glow discharge. The presence of the dielectric in the discharge gap led to the discharge quenching and thus the decay of the plasma. Additionally, the argon metastable density was monitored by measuring light emission from nitrogen impurities. A metastable density of about 5×10^{17} m^{-3} was present during the entire voltage cycle, with only a small ($\sim$10%) increase during the discharge. Finally, a reduction of the applied voltage to the minimum required to sustain the discharge led to a further reduction of the role of the dielectric. The discharge was no longer quenched by the dielectrics only but also by a reduction of the applied voltage.

1. Introduction

A dielectric barrier discharge (DBD), sometimes referred to as a barrier discharge or a silent discharge, is a type of discharge in which at least one of the electrodes is covered with a dielectric material. This dielectric layer acts as a current limiter and prevents the formation of a spark or an arc discharge. The electrical energy coupled into a DBD-plasma is mainly transferred to energetic electrons, while the neutral gas remains close to ambient temperatures. The non-equilibrium plasma that is produced can be operated at elevated pressures (10^4–10^6 Pa). This combination of plasma properties makes it a unique device with many industrial applications.

DBDs have been extensively studied for over a century. Their principles have been thoroughly investigated and are described in numerous papers, for example [1–4]. Traditional industrial applications range from ozone synthesis in oxygen and air to cleaning of flue gases. Nowadays, DBDs are also used in plasma display panels, high-power CO_2 lasers and excimer UV/VUV lamps [3].

For most operating conditions, a DBD consists of a (large) number of discharge filaments, which have a nanosecond duration and are randomly distributed over the dielectric surface. These filaments, also known as microdischarges, are the active regions of a DBD in which active chemical species and UV/VUV radiation can be produced. These microdischarges act as individual discharges which work independently of one another. The discharge dynamics and chemistry of individual microdischarges have been studied in detail, both through modelling and experimental investigations [5–7].

In the 1980s, a different type of discharge mode in DBDs was observed [8, 9]. Under certain operating conditions, the discharge appears as a diffuse glow, covering the entire electrode surface uniformly. Since then numerous investigations have been performed to understand and explain the physical basis of this discharge mode. Several mechanisms have been discussed to explain the generation of diffuse DBDs. These include gas pre-ionization by electrons or metastables from previous discharges [10, 11] and interaction between the plasma and the dielectric surfaces [12–14].

Since atmospheric pressure conditions are most suitable for many DBD applications, the research on the properties of the different discharge modes has focused mainly on atmospheric pressure conditions rather than on the low-pressure regime. However, a detailed description of the behaviour of DBDs at low pressure may contribute to a better understanding of the fundamental processes involved in DBDs. Especially the knowledge of the plasma breakdown mechanisms, including the role of the (charged) dielectric surfaces herein, can benefit from an investigation of low-pressure DBDs (LPDBDs).

The aim of the research described in this paper is to investigate the behaviour of a LPDBD in 400 Pa argon gas. We characterized the discharge properties by recording voltage and current waveforms and by measuring plasma emission spectrally, spatially and temporally resolved. For a better understanding of the discharge phenomena observed, we compared the experimental results with calculations from a two-dimensional fluid model.

This paper is structured as follows. Section 2 contains a description of the discharge apparatus and the diagnostic system. In section 3, we briefly describe the two-dimensional fluid model used for our simulations. The results of the electrical and emission experiments are presented in section 4. In this section, these results are also compared with the results of the calculations from the two-dimensional model. Section 5 contains a discussion of the results, focusing on the role of the dielectric materials in the discharge behaviour. Further, a simple comparison is made between our current results and similar well-known discharges at high and low pressure. Finally, section 6 contains a brief summary of the main conclusions and an outlook.

2. Experimental arrangement

The experimental arrangement consisted of a discharge apparatus, which is described in section 2.1, and a set of diagnostics, described in section 2.2. The experimental arrangement has previously been used for cross-correlation spectroscopy on DBD-microdischarges and diffuse DBDs at atmospheric pressure [6, 15].

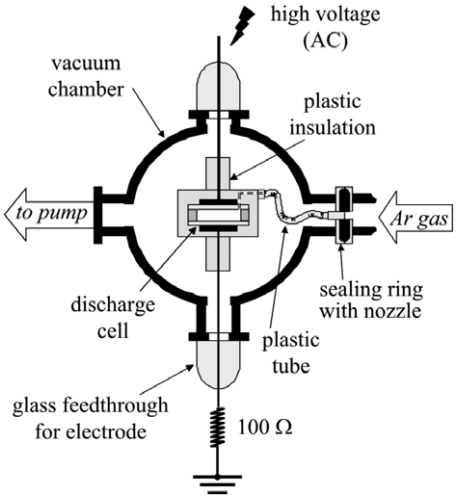

Figure 1. Schematic diagram of the discharge apparatus.

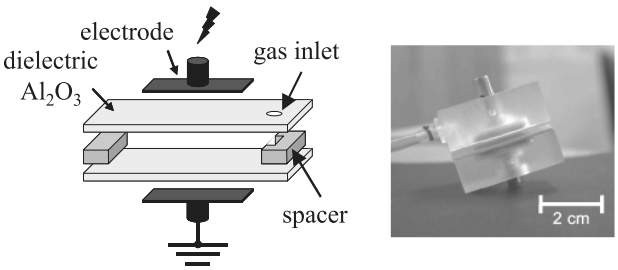

Figure 2. Schematic diagram and photograph of the discharge cell. The size of the electrodes was 20 mm × 20 mm and the thickness of the Al_2O_3 dielectric layer was 0.7 mm. The spacer, determining the size of the discharge gap, had a thickness of 5.0 mm. The photograph on the right shows the discharge cell embedded in a block of plastic for insulation purposes.

2.1. Discharge apparatus

The discharge apparatus consisted of a vacuum chamber, power supply and electrode arrangement. Figure 1 shows a schematic diagram of the discharge apparatus.

The actual DBD was created in the discharge cell. Details of this cell are presented in figure 2. The discharge cell was made up of two identical square (20 mm × 20 mm) electrodes, covered with dielectric material (Al_2O_3). A spacer, made of glass, connected the two electrodes together, creating a 5.0 mm discharge gap. Gas entered the discharge region through the gas inlet in the top dielectric plate. The total argon flow was 140 sccm, resulting in a gas flow in the discharge cell with a velocity of about 3 m s^{-1}, thus a laminar flow can be assumed.

The discharge cell was mounted in the centre of a vacuum vessel. The vessel was evacuated by a rotary vane pump, creating a residual pressure of about 0.5 Pa. A continuous flow of argon gas (purity 99.999%) was directed through the system. The gas flow was controlled by a flow controller, which maintained the pressure in the vessel at 400 Pa. The argon gas entering the vacuum vessel was introduced directly into the discharge volume. A sealing ring with a nozzle on the

entrance window of the vessel directed the argon flow through a plastic tube to the discharge cell.

To generate the discharge, a sinusoidal alternating voltage was applied to the electrodes. A sinusoidal waveform from a function generator was amplified first with an audio-amplifier and subsequently with an ignition coil. The resulting voltage typically had a peak-to-peak amplitude of several hundreds of volts and a frequency of 5–15 kHz. Two feedthrough windows, made of glass, were used to supply the voltage from the voltage source to the electrodes inside the vacuum chamber. The discharge cell in the chamber was embedded in a block of plastic insulation to prevent discharges between the electrode wires and the wall of the vessel.

2.2. Diagnostic system

The behaviour of the discharge was studied using a diagnostic system that could characterize both the electrical properties and the light emission of the plasma.

2.2.1. Electrical properties. The electrical behaviour of the discharge was characterized by measuring the applied voltage and the discharge current. The high voltage applied to the electrodes was measured using a 1000 : 1 voltage probe. The discharge current was monitored by measuring the voltage across a 100 Ω resistor, connected in series with the discharge cell. Both waveforms were simultaneously recorded on a digital oscilloscope.

During a discharge cycle, the externally applied voltage, V_a, consisted of a voltage difference across the gas gap, V_g, and a voltage across the dielectric barrier plates, V_b. The gap voltage, V_g, and the barrier voltage, V_b, could be calculated from the recorded applied voltage and current using the following relations [11]:

$$V_g(t) = V_a(t) - V_b(t), \tag{1}$$

$$V_b(t) = 2/C_b \int_{t_0}^{t} I_d(t')\,dt' + V_b(t_0), \tag{2}$$

where C_b is the capacitance of a single dielectric plate, $I_d(t')$ the recorded discharge current, $V_b(t_0)$ the voltage due to charges on the dielectric surfaces that were left over from the previous discharge cycle and t_0 the starting time of the voltage cycle. The value of $V_b(t_0)$ is chosen such that there is no auto-polarization. This means that the mean value of the gas voltage, V_g, over a full voltage cycle is equal to 0 V. The value of C_b was calculated to be 50.6 pF, taking the relative dielectric constant for Al_2O_3, ϵ_r, equal to 10, a thickness of 0.7 mm for the dielectric plates and a size of 20 mm × 20 mm for the electrodes.

2.2.2. Plasma light emission. The aim of measuring the plasma light emission was to investigate the dynamic behaviour of the discharge. The main part of this diagnostic system was a highly sensitive photomultiplier (Hamamatsu HS5773-04) and a single-photon counting (SPC) module (Becker and Hickl SPC-530). This system was capable of detecting single photons, which made it possible to study the weak plasma emission with an adequate spatial, temporal and spectral resolution. A movable lens system provided the spatial resolution, a monochromator spectral resolution and a pattern generator temporal resolution. Each of these subsystems will be discussed in more detail in the rest of this section.

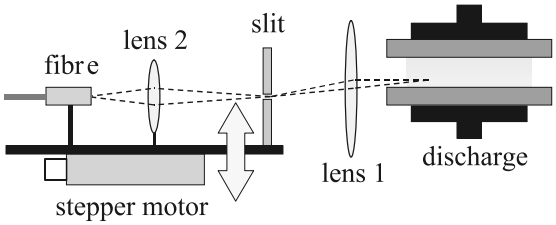

Figure 3. Optical system for one-dimensional spatially resolved emission measurements, consisting of two lenses, a slit, a stepper motor and an optical fibre. The stepper motor was used to move the slit vertically, which changed the area in the discharge that was studied.

The optical system, shown in figure 3, was used to obtain one-dimensional spatially resolved measurements. It consisted of two lenses, a slit, a stepper motor and an optical fibre. Light emission from the discharge was imaged onto a slit by lens 1. Part of the light emission passed through the slit and was focused onto an optical fibre leading to a photon detector. The vertical position of the slit determined the area in the plasma that was measured. The slit, together with lens 2 and the fibre, was moved vertically by a stepper motor, allowing the measurement of a one-dimensional emission profile across the discharge gap. The spatial resolution for our experiments was 0.5 mm and was determined by the width of the slit.

Plasma light emission that was focused onto the optical fibre, as described above, was sent through a monochromator. Depending on the width of the monochromator entrance slit, a spectral resolution of 0.2–1.5 nm was achieved.

After the spatial and spectral selection, the remaining signal from the plasma was very weak, consisting only of single photons per discharge cycle. A highly sensitive photomultiplier, with a gain of 10^6 and operating in a single photon detection mode was used to detect the spatially and spectrally resolved plasma emission. The photomultiplier was cooled down to +10 °C to increase the signal-to-noise ratio.

A temporal resolution of up to 400 ns was achieved using a computer pattern generator (Becker and Hickl, PPG-100). This device created a pattern of 512 consecutive time bins of 400 ns each, corresponding to 512 segments in the computer memory. The start of the pattern was synchronized with the applied voltage waveform, dividing a single voltage cycle into about 357 bins of 400 ns. During each measurement, the detection of a photon by the photomultiplier was stored in the corresponding segment of the computer memory. Typically, signals from up to 10^7 discharge cycles were accumulated in the memory, which reconstructed the temporal development of the discharge during a single voltage cycle.

The SPC module was originally designed for use in cross-correlation spectroscopy. An example of the application of this technique to DBD microdischarges in atmospheric air can be found in [6]. For our measurements, the experimental setup was modified as described in [15, 16]. The SPC module was triggered by the pattern generator, which made the SPC module act as a 'simple' photon counter oscilloscope. Time resolution in our measurements was provided by the pattern generator

and proved sufficient to resolve the dynamic behaviour of the discharge emission.

3. Two-dimensional fluid model

For comparison with experiments, we employed a time-dependent, two-dimensional fluid model. In our plasma the mean free paths for electrons and ions are about 100 μm and 25 μm, respectively. These characteristic lengths are much smaller than the discharge dimensions. Therefore, the LPDBD can be described by a fluid model. Our model was originally developed for use in plasma display technology [17] and was later adapted to describe breakdown phenomena in long fluorescent tubes [18]. A detailed description of the model can be found in [18] and references therein. Here, only the basic features of this model, in particular the species and reactions that were included as well as the numerical approximation of the discharge geometry, are described.

3.1. Model equations

Following conventional fluid models, our model was based on balance equations, derived from the Boltzmann transport equation, and on the Poisson equation. The balance equations were solved for a number of species using the drift–diffusion approximation. The species included in the model, such as electrons, ions and excited atoms, are described in more detail in section 3.2. The balance equations for the different species were

$$\frac{\partial n_p}{\partial t} + \nabla \cdot \boldsymbol{\Gamma_p} = S_p, \tag{3}$$

with $\boldsymbol{\Gamma_p}$ being the drift–diffusion flux,

$$\boldsymbol{\Gamma_p} = \pm \mu_p \boldsymbol{E} n_p - D_p \nabla n_p, \tag{4}$$

where n_p is the density of species p, S_p the source term of species p due to reactions, μ_p the mobility, D_p the diffusion coefficient of species p and $\boldsymbol{E}$ the electric field.

In order to specify the various reaction rate coefficients and electron transport coefficients as functions of the mean electron energy, an additional balance equation for the electron energy was included:

$$\frac{\partial (n_\mathrm{e} \bar{\varepsilon})}{\partial t} + \nabla \cdot \boldsymbol{\Gamma}_{\bar{\varepsilon}} = S_{\bar{\varepsilon}}, \tag{5}$$

in which $\bar{\varepsilon}$ is the average electron energy and n_e the electron density. The source term of this equation, $S_{\bar{\varepsilon}}$, represents the energy gained in the electric field and the energy lost in collisions. The electron energy flux, $\boldsymbol{\Gamma}_{\bar{\varepsilon}}$, is described by [19]

$$\boldsymbol{\Gamma}_{\bar{\varepsilon}} = -\frac{5}{3} \mu_\mathrm{e} \boldsymbol{E} n_\mathrm{e} \bar{\varepsilon} - \frac{5}{3} n_\mathrm{e} D_\mathrm{e} \nabla \bar{\varepsilon}, \tag{6}$$

in which the first term on the right-hand side is the hydrodynamic flux of enthalpy and the second term the heat conduction flux. This approach differed from the commonly used local field approximation, in which these coefficients are specified as a function of the local electric field.

The actual electron transport and reaction rate coefficients were pre-calculated by a Boltzmann solver [20]. The solver calculates the electron energy distribution function at different reduced electric fields. From this, the electron transport and reaction rate coefficients were calculated as a function of the mean electron energy. The resulting data set was used to create a lookup table to be used as input for the model.

The transport coefficients for species other than the electrons and the reaction rate coefficients for heavy particle reactions were found in the literature and were used as input for the model as a function of the reduced electric field. Details on the values and origins of these coefficients can be found in section 3.2.

Finally, in addition to the balance equations discussed above, the Poisson equation was solved:

$$\nabla \cdot (\epsilon \nabla \varphi) = -\nabla \cdot (\epsilon \boldsymbol{E}) = -\sum_p q_p n_p, \tag{7}$$

in which φ is the electric potential as a function of position and time, ϵ is the permittivity of the medium and q_p the charge of the species p. From this the electric field and potential distribution in the discharge area were determined.

For each time step, all equations of the model were solved on a rectangular, uniform grid, using a control volume method [21].

3.2. Species and reactions

The set of species used in the model consisted of electrons, e, argon ions, Ar^+, molecular argon ions, Ar_2^+, and three effective excited states of argon atoms. The first effective excited state, called Ar^*, represented the four 4s levels of the argon atom. This species Ar^* was assumed to be metastable because the electron impact cross section for creating a metastable 4s state is significantly larger than the cross section for the creation of a resonant 4s state. Next, all excited atoms in 4p and higher levels were grouped together in the second effective excited state, Ar^{**}. Finally, a third excited species, Ar_r^*, was used in the model. This species was introduced to take into account collisional quenching from the two metastable 4s states to the two resonant 4s levels. The species Ar_r^* were lost by deexcitation to the ground level. Details about the choice of the different species used in the model can be found in [18].

The transport coefficients for the different species were taken from the literature [20,22–24]. For the charged particles the diffusion coefficients were calculated from the mobilities using the Einstein relation [19]. At the dielectric walls, the incoming electrons were absorbed and charged up the wall. The incoming heavy particles were neutralized or deexcited. The resulting ground state atoms were reflected back into the plasma. Part of the incoming particles caused secondary electron emission at the dielectric wall. The secondary emission coefficients for Ar^+, Ar_2^+ and Ar^* depend strongly on the properties of the dielectric surface and are not exactly known. We used values of 0.02 for Ar^+ and Ar_2^+ and 0.01 for Ar^*. More details on the boundary conditions of the model can be found in [18].

The set of reactions between the species that were included in the model is listed in table 1. Note that the reaction rate coefficients for reactions which include electrons were calculated using a Boltzmann solver.

Finally, electron–electron collisions were not included in the model. This is because inelastic collisions between electrons and the background gas were more common than electron–electron collisions since the ionization degree of the plasma under study was low.

Table 1. Reactions included in the model. The third column contains references to the original literature from which the cross sections or rate coefficients were taken.

No	Reactions	References
0	$Ar + e \rightarrow Ar + e$	[25]
1	$Ar + e \rightarrow Ar^{*} + e$	[26]
2	$Ar + e \rightarrow Ar^{**} + e$	[26]
3	$Ar + e \rightarrow Ar^{+} + 2e$	[25]
4	$Ar^{*} + e \rightarrow Ar + e$	[26][a]
5	$Ar^{*} + e \rightarrow Ar^{**} + e$	[27]
6	$Ar^{*} + e \rightarrow Ar^{+} + 2e$	[28]
7	$Ar^{**} + e \rightarrow Ar + e$	[26][a]
8	$Ar^{**} + e \rightarrow Ar^{*} + e$	[27][a]
9	$Ar^{**} + e \rightarrow Ar^{+} + 2e$	[29]
10	$Ar^{*} + Ar^{*} \rightarrow Ar^{+} + Ar + e$	[30]
11	$Ar^{*} + Ar^{**} \rightarrow Ar^{+} + Ar + e$	[30]
12	$Ar^{**} + Ar^{**} \rightarrow Ar^{+} + Ar + e$	[30]
13	$Ar^{*} + e \rightarrow Ar_{r}^{*} + e$	[31, 32]
14	$Ar_{r}^{*} \rightarrow Ar + h\nu$	[18]
15	$Ar^{**} \rightarrow Ar^{*} + h\nu$	[18]
16	$Ar^{+} + 2Ar \rightarrow Ar_{2}^{+} + Ar$	[33]
17	$Ar_{2}^{+} + e \rightarrow Ar^{*} + Ar$	[34]

[a] From the forward reaction using microscopic reversibility.

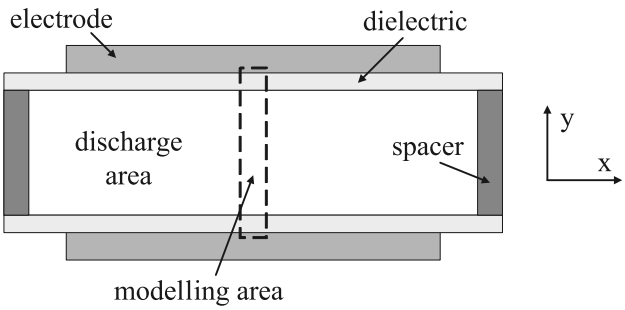

Figure 4. Schematic diagram of the discharge geometry and modelling area.

3.3. Discharge geometry

The experimental discharge geometry is schematically shown in figure 4. The dashed box indicates the part of the discharge that was described by the model. Since experiments showed that at low pressures the discharge was homogeneous along the x direction, we decided to only include the centre of the discharge area in the model. On this discharge area, a numerical grid in Cartesian coordinates was defined, consisting of 93 points in the y direction and 15 points in the x direction.

The initial condition for the electrons and the ions was a homogeneous density of 10^{13} m^{-3}. The metastable states also had an initial density of 10^{13} m^{-3}. With these initial conditions, the modelled discharge needed several voltage cycles to reach a reproducible discharge for each voltage cycle.

4. Experimental and modelling results

In this section, we present the results of our experimental and modelling investigations. Measurements of the electrical properties of the discharge and the plasma light emission are compared with calculations from our fluid model. Experiments showed that at a relatively high voltage (700 V_{pp}), a transient, glow-like discharge developed. By reducing the amplitude of the applied voltage (440 V_{pp}) we could observe changes in the discharge dynamics. Section 4.1 focuses on the properties of the transient, glow-like discharge, whereas section 4.2 deals with the effects of reducing the operating voltage.

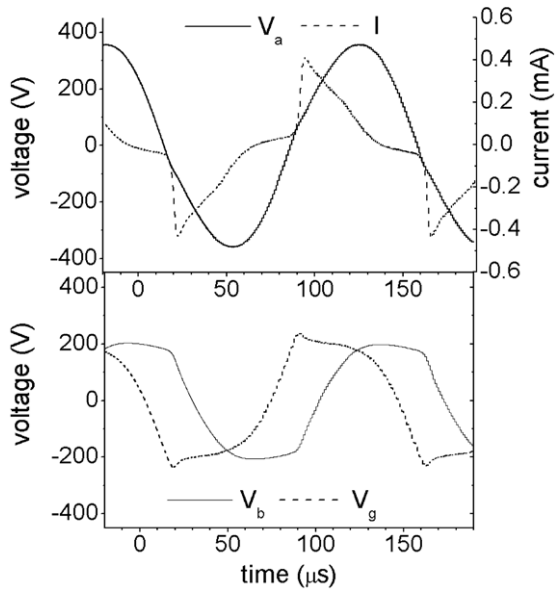

Figure 5. Measurements of the applied voltage, V_a, and discharge current, I, in the LPDBD in argon. The voltages across the dielectric plates, V_b, and the gas gap, V_g, were calculated from the measured voltage and current following the procedure outlined in section 2.2.1.

4.1. Transient glow-like discharge

A discharge in 400 Pa argon gas was created by applying a sinusoidal voltage with a frequency of 7 kHz and an amplitude of 700 V_{pp}. The plasma appeared diffuse, covering the entire electrode surface.

4.1.1. Electrical properties. An electrical characterization of the discharge is presented in figure 5. The applied voltage, V_a, and discharge current, I, were measured and the voltages across the gas gap, V_g, and the dielectric barriers, V_b, were calculated using equations (1) and (2). The discharge current waveform shows that the discharge consisted of a single discharge per voltage half-cycle with a duration of about 40 μs. The similar shape of the positive and negative current pulse indicated that the discharge was similar for both voltage polarities.

The barrier voltage, V_b, and the gap voltage, V_g, show that the discharge started when the amplitude of the gas voltage rose above the breakdown voltage of the discharge gap ($t = 18\,\mu$s). Within a few microseconds the discharge current rose to its maximum ($t = 21\,\mu$s). At this point, V_g dropped slightly (about 20 V) and subsequently, over the next 30 μs, the discharge current decreased to zero, while V_g remained almost constant. During this time, the increasing applied voltage amplitude led to an increase of V_b. After the maximum in V_a ($t = 55\,\mu$s), the voltage, V_b remained constant, while V_g dropped when the applied voltage amplitude was decreased. Next, V_g changed polarity ($t = 75\,\mu$s), now opposing V_b.

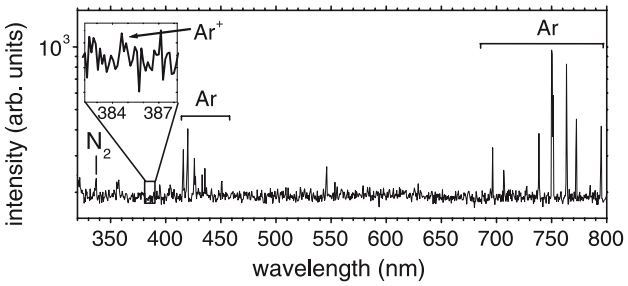

Figure 6. Spectrum of plasma emission. In the wavelength range from 690 to 800 nm, several spectral lines of 4p to 4s transitions in atomic argon could be identified. Further, 5p to 4s transitions in atomic argon were detected for wavelengths between 400 and 500 nm. Additionally, a weak ionic argon line was identified at 385.0 nm and a spectral band of the second positive system of nitrogen (0–0 transition) at 337.1 nm was observed.

Shortly after the polarity change of the applied voltage, V_g reached the breakdown voltage again and a new discharge, with opposite polarity, was initiated ($t = 91\ \mu$s).

The electrical behaviour of the LPDBD is consistent with most of the typical characteristics of DBDs at atmospheric pressure, especially with diffuse DBDs. The discharge ignites when the voltage across the gas gap rises above the breakdown voltage. The gas in the discharge gap breaks down, a plasma is formed and the discharge current rises steeply. During the discharge, charged particles produced in the plasma are deposited on the dielectric surfaces in front of the electrodes, creating an electric field opposing the applied electric field. The resulting total electric field in the gap decreases and the discharge extinguishes. The charges remain on the dielectrics after the discharge ends and cause a residual electric field for the next discharge. After a polarity change of the applied voltage, V_b now enhances the applied voltage and a discharge of opposite polarity can be initiated at relatively low applied fields.

4.1.2. Spectral characterization. For the characterization of the light emission of the discharge we recorded a time and space-integrated emission spectrum, which is shown in figure 6. The emitted plasma light consisted mainly of atomic argon lines. Additionally, the spectrum revealed the presence of argon ions and nitrogen molecules in the plasma. The nitrogen emission was probably due to residual gas in the chamber or impurities in the argon gas. From the spectrum in figure 6, three emission lines were chosen for further spatio-temporal investigation. First, the strong atomic argon line at 750.4 nm was chosen to characterize the general discharge behaviour. Second, the ionic argon line at 385.0 nm was used to investigate ionization processes and the presence of ions during the discharge. Finally, the nitrogen band at 337.1 nm was measured to study the effect of impurities in the discharge.

4.1.3. Spatio-temporal structure of plasma emission. Figure 7 presents the results of the spatio-temporally resolved emission spectroscopy at 750.4 nm. The discharge started with some weak light emission in front of the anode ($t = 10\ \mu$s). Subsequently, a fast light front crossed the discharge gap from the anode towards the cathode ($t = 18\ \mu$s). The moving

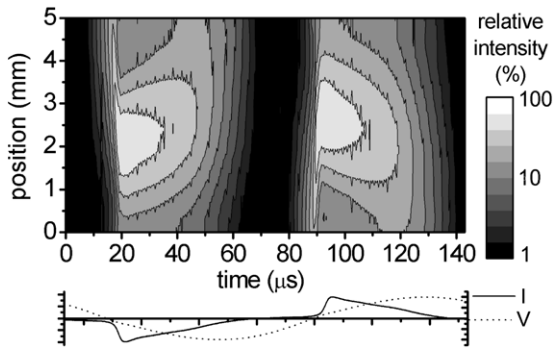

Figure 7. Spatially and temporally resolved measurements of plasma light with a wavelength of 750.4 nm (atomic argon, 4p–4s transition). The dielectric surfaces were located at positions 0 and 5 mm. The measured applied voltage and current are shown under the graph. The voltage was applied to the lower electrode in the figure, which made it the cathode during the first voltage half-cycle and the anode during the second.

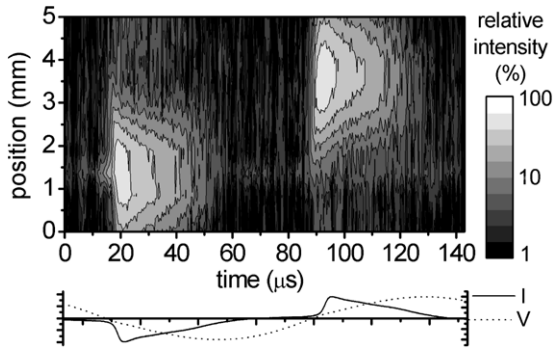

Figure 8. Spatially and temporally resolved measurements of plasma light with a wavelength of 385.0 nm (ionic argon). The dielectric surfaces were located at positions 0 and 5 mm. The measured applied voltage and current are shown under the graph. The voltage was applied to the bottom electrode.

front had an average velocity of approximately 1700 m s^{-1}. The light front did not reach the cathode completely; it stopped at about 2 mm in front of the cathode. Next, a stable light distribution developed in the discharge gap, consisting of an emission region with a width of about 2 mm and a maximum situated at about 2 mm from the cathode ($t = 20\ \mu$s). This stable discharge light distribution existed in the gap for 15 μs after which it extinguished in the next 30 μs. In the following period ($t = 60$–$80\ \mu$s) there was no measurable light emission. Subsequently, a new discharge started with the same characteristics as the previous one but with an opposite polarity.

An investigation of the spatio-temporal behaviour of argon ions during the discharge is presented in figure 8. Argon ion line emission with a wavelength of 385.0 nm was measured. This light emission is most likely to come from ions which were excited by direct electron impact excitation. The general discharge behaviour for the ions is very similar to the behaviour of the atomic argon light emission. A light front travelled from the anode to the cathode with a velocity of about 1700 m s^{-1}. Subsequently, a stable discharge developed during the following 5 μs after which the ion light emission died out. One of the differences between the atomic light emission

(figure 7) and the ionic light emission (figure 8) was the starting point of the moving light front. The atomic emission started at the anode surface, while the ionic emission started at about 1 mm in front of the anode. Furthermore, the ionic emission decayed faster than the atomic light and it had a maximum which was located 0.5 mm closer to the cathode than the atomic emission.

Since the lifetime of the excited states of argon ions and atoms is in the order of nanoseconds, the measured plasma emission can be interpreted as regions of considerable excitation. Furthermore, the difference in the required energy for excitation and ionization is small for argon. Therefore, the measurements in figures 7 and 8 can be interpreted as an ionization wave crossing the discharge gap during the breakdown phase, a stable glow-like discharge in the subsequent phase and a decaying plasma in the final phase. The concept of the development of a moving ionization wave could also explain some of the differences between the ionic (figure 8) and atomic (figure 7) argon emission. The electric field strength in a moving ionization front that is crossing the discharge gap will increase with time [35]. As a result the average electron energy in the wave will also increase. Because the excitation energy of the argon ions (20.0 eV) is higher than that of the argon atoms (13.3 eV), the ionic argon emission will be observed in a more developed phase of the ionization wave, which is closer to the cathode.

The breakdown phase (t = 10–20 μs) of the discharge agrees with the well-known Townsend breakdown mechanism [19], which describes discharge ignition for low-pressure discharges. Townsend theory is based on the development of electron avalanches driven by an electric field present in the discharge gap. Successive generations of electron avalanches are generated by secondary electron emission at the cathode, due to ion bombardment. Since the ion mobility is much smaller than the mobility of the electrons, a positive space-charge region develops in front of the anode. This space-charge modifies the electric field distribution in the gap, leading to the formation of a glow discharge, including features such as the cathode fall region, negative glow and Faraday dark space.

The effect of the dielectric plates was limited during the breakdown phase of the discharge, since the breakdown mechanism was equivalent to the well-known low-pressure glow plasmas without dielectrics [35]. But when the discharge burnt for a few microseconds, the charging of the dielectrics caused the discharge extinction. This was not observed in a normal glow-discharge between metal electrodes.

The presence of nitrogen impurities in the discharge was monitored by measuring light emission from the second positive system of N_2 at 337.1 nm. The results of these measurements, shown in figure 9, reveal a different behaviour compared with the argon line emission. There was a continuous nitrogen emission in the entire discharge gap, with a maximum in the centre. During the discharge the maximum emission slightly increased (about 10%), but it did not decay completely during the decay phase of the plasma. The reason for different structures of the nitrogen plasma emission is most likely the excitation of the N_2(C) level by argon metastables. The energy of the argon metastables (11.6 eV) can be resonantly transferred to nitrogen molecules, exciting the second positive system (excitation energy 11.0 eV). Since

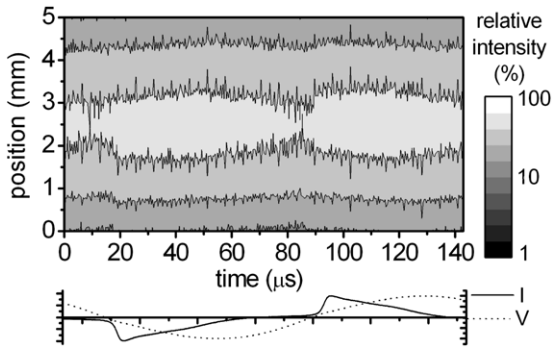

Figure 9. Spatially and temporally resolved measurements of plasma light with a wavelength of 337.1 nm (molecular nitrogen, 2nd positive system). The dielectric surfaces were located at positions 0 and 5 mm. The measured applied voltage and current are shown under the graph. The voltage was applied to the bottom electrode.

the excited state lifetime is in the order of nanoseconds, the nitrogen emission indicates the presence of argon metastables. The metastables were produced during the discharge but remained in the discharge volume during the entire voltage cycle. The spatio-temporally resolved development shown in figure 9 implies that the metastable density at the onset of the breakdown process is about 90% of the maximum density during the discharge of the previous voltage half-cycle.

4.1.4. Modelling results. The fluid model described in section 3 was used to simulate the LPDBD. The output of the model consisted of time-dependent, two-dimensional maps of plasma properties such as particle densities, reaction rates, potential and electric field. The full two-dimensional results showed no radial dependences of the calculated plasma properties. Therefore, a single axial profile was used to represent the characterization of the whole discharge. In figure 10, the model calculations of the discharge voltages are compared with the experimental measurements. The maximum in V_g, which corresponds to the breakdown voltage of the discharge, was calculated to be 235 V. This was within 5% of the measured breakdown voltage.

The experimental spatio-temporal investigations of the light emission of the discharge, shown in figure 7, were compared with the time-dependent reaction rate of reaction 15 in table 1. This reaction represents the decay of all excited argon atoms in levels 4p and higher into the 4s level and can be interpreted as a large part of the total light emission. In the experiments, a single 4p–4s transition was measured at 750.4 nm. The spatio-temporal behaviour of the calculated reaction rate is presented in figure 11. The model predicts a single discharge per voltage half-cycle, as was seen in the experiments. Furthermore, the calculated results also show a cathode-directed moving light front and a stable discharge with maximum light emission in front of the cathode. However, in the experiments, the moving light front started at the anode surface, while in the calculations it was initiated about 1 mm in front of the anode. Furthermore, the maximum in the light emission during the discharge phase (25–45 μs) was closer to the cathode in the calculations than in the experiments. These discrepancies in the starting point of the moving front and the position of the maximum of the light emission might be

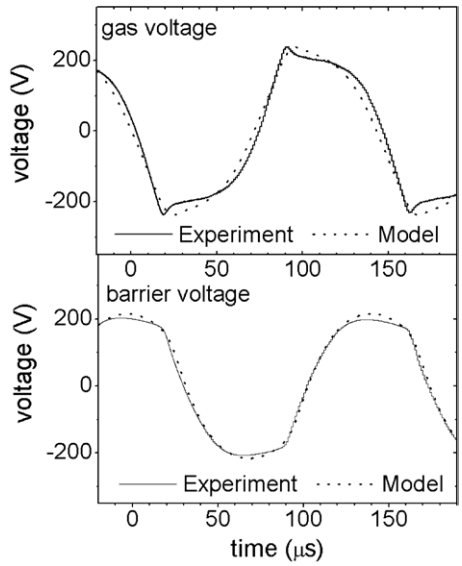

Figure 10. Comparison of the modelling results with the experimental data on the discharge voltages. The top figure shows the gas voltage, V_g; the bottom figure shows the voltage across the barrier, V_b. The solid lines are experimental data, the dotted lines the modelling results.

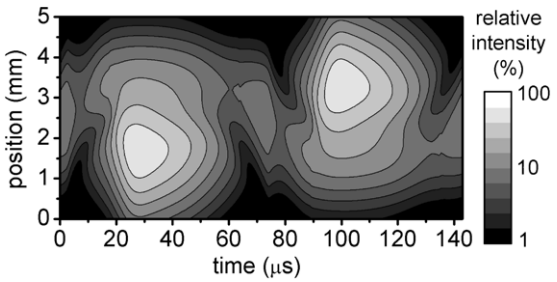

Figure 11. Spatio-temporal development of the calculated rate of the reaction $Ar^{**} \rightarrow Ar^{*} + h\nu$ (table 1). This reaction rate can be interpreted as the main part of the total light emission (cf figure 7). The dielectric surfaces were located at positions 0 and 5 mm. The voltage was applied to the lower electrode in the figure, which made it the cathode during the first voltage half-cycle and the anode during the second.

due to surface processes on the dielectrics, such as electron desorption and photoemission, which are not included in the model. The importance of such surface processes in the discharge behaviour of DBDs has been established [12, 14]. However, the exact mechanisms and relative importance of the different surface processes are not yet fully understood. Therefore, further investigations are needed to identify which processes are important and what their exact influence on the discharge behaviour of the LPDBD will be. Finally, during the time in between two discharges (60–80 μs) there was no light emission at 750.4 nm measured in the experiments, while there was still some emission according to the calculations. Despite these differences the main discharge characteristics were reproduced by the model.

To investigate the plasma structure during the discharge phase, the calculated potential distribution, axial electric field and particle densities at the time of maximum light emission ($t = 30\,\mu$s) are shown in figure 12. The potential and

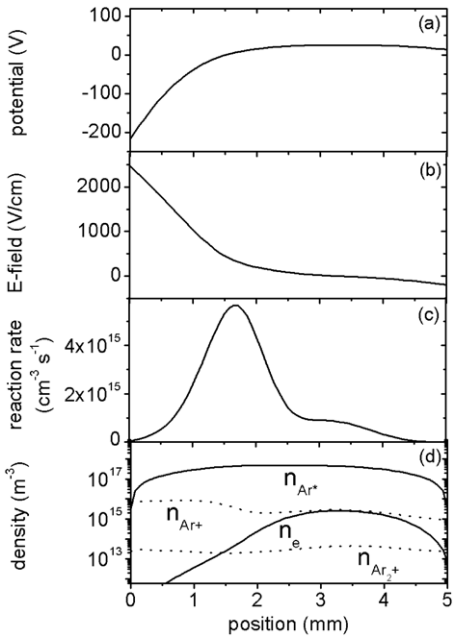

Figure 12. Model calculations of the stable glow phase at $t = 30\,\mu$s. The figure shows the distributions in the discharge gap of the potential (*a*), electric field (*b*), $Ar^{**} \rightarrow Ar^{*} + h\nu$ reaction rate (*c*) and particle densities (*d*). The cathode is positioned at $x = 0$ and the anode at $x = 5$.

electric field distributions showed the formation of a cathode fall region with a thickness of about 1.5 mm. In this region, the potential fall was about 215 V and the electric field had a maximum of 2500 V cm^{-1}. Additionally, in this region, the argon ion density was several orders of magnitude higher than the electron density, creating a positive space-charge. The reaction rate shown in figure 12(*c*), which can be interpreted as plasma light emission, indicated that the cathode region was a region, without significant excitation of argon atoms. The characteristics of this layer ($x = 0$–1.5 mm) are similar to the properties of a cathode sheath region in a conventional, low-pressure dc glow discharge.

The region between the positions 1–2.5 mm showed considerable light emission (figure 12(*c*)) but a low electric field. These properties are similar to the negative glow region of a glow discharge. Finally, the region $x = 2.5$–5 mm was again a dark region, which was almost charge neutral and had a low electric field. Because the gas gap was relatively small, there was no formation of a positive column, as is the case in a dc glow in a long tube.

The calculated plasma structure during the discharge phase, presented in figure 12, shows several features similar to the well-known, low-pressure glow discharge. Furthermore, the breakdown phase of the LPDBD was also similar to the Townsend breakdown process, known from standard glow discharges. This indicates that the discharge behaviour of the LPDBD can be interpreted as a transient glow-like discharge.

Figure 12(*d*) shows an almost homogeneous metastable density of about 5×10^{17} m^{-3} in the discharge gap. This density was present during the entire voltage cycle, with only a small increase (∼10%) during a discharge, which is in agreement with the results shown in figure 9. At the start of the breakdown phase of the discharge, the metastable

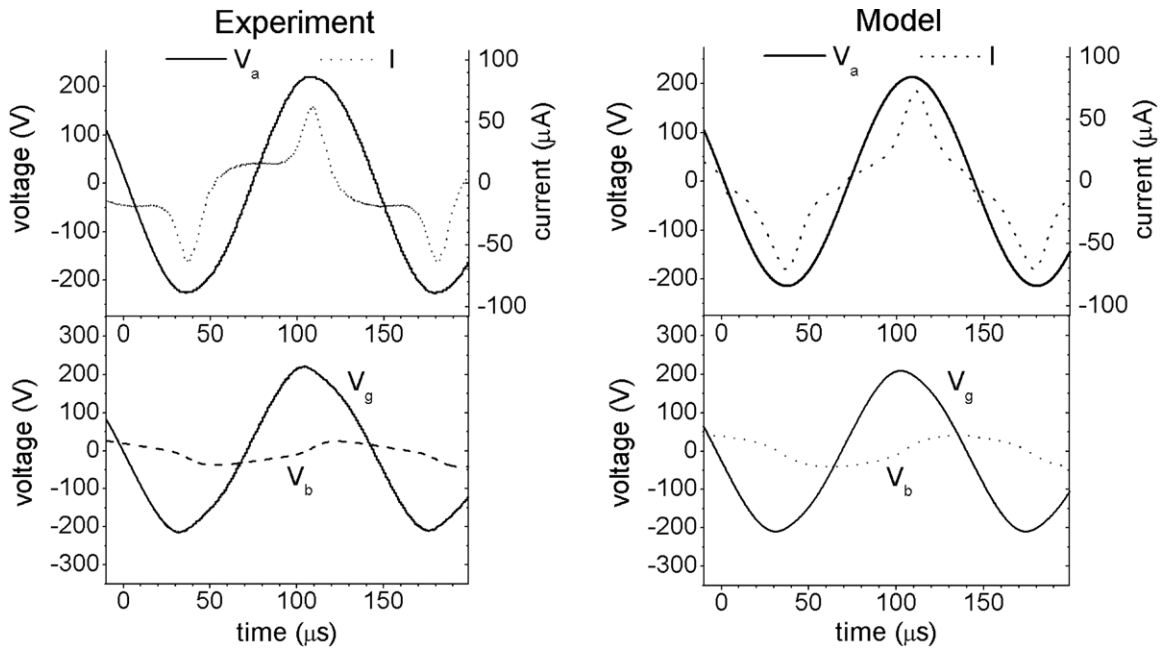

Figure 13. The left part of the figure shows measurements of the applied voltage and discharge current in the LPDBD at an applied voltage of 440 V_{pp}. The voltages across the dielectric plates, V_b, and the gas gap, V_g, were calculated from the measured voltage and current following the procedure outlined in section 2.2.1. The right part of the figure shows the results of the model calculations.

atoms can play an important role. Through processes such as metastable–metastable collisions (reactions (10)–(12), table 1), the metastables provide extra electrons that create electron avalanches and influence the behaviour of the breakdown process. In between the discharges, at time $t = 70\,\mu$s, ionization due to metastable–metastable collisions is about an order of magnitude higher than ionization due to electron impact.

4.2. Effect of reducing the applied voltage amplitude

Lowering the applied voltage of the discharge to 440 V_{pp} caused changes in the discharge behaviour of the glow-like discharge mode. In the following section, we will characterize the discharge at 440 V_{pp} and compare it with the discharge at 700 V_{pp} as discussed in the previous section.

4.2.1. Electrical properties. Starting with a discharge at 700 V_{pp}, decreasing the voltage amplitude resulted in a continuously changing shape of the current waveform. The discharge current amplitude decreased and the discharge occurred at a later time in the voltage cycle. At the minimum voltage required to sustain the discharge (440 V_{pp}), the current amplitude was 60 μA and the peak position was close to the maximum of the applied voltage cycle. The measured voltage and current for this minimum applied voltage case are presented in figure 13. Although the applied voltage amplitude was 35% lower than before, the maximum gas voltage, V_g, was approximately equal to the situation with higher applied voltage (figure 5). This implies that discharge ignition occurred at the same breakdown voltage as before. However, because the breakdown voltage was reached later in the voltage cycle, there was not enough time to build up a fully developed plasma and a significant barrier voltage, V_b, during the discharge. As soon as V_a reached its maximum value and subsequently started to decrease, the discharge could no longer be sustained and extinguished.

4.2.2. Spatio-temporal structure of plasma emission. Figure 14 shows measurements of plasma emission of atomic argon at 750.4 nm. The discharge behaviour was significantly different from the 700 V_{pp} situation presented in section 4.1. Again, the first plasma emission was seen in front of the anode ($t = 10\,\mu$s), but no moving, cathode-directed light front was observed. Instead, the maximum of the light emission remained in front of the anode during the entire voltage cycle. When the voltage increased, the light emission also increased, maintaining the axial shape of the light distribution inside the gap. After the maximum in the applied voltage ($t = 38\,\mu$s), the discharge extinguished in the next 20 μs.

The results of the calculations of the fluid model for the electrical characteristics are shown in figure 13 and for the plasma light emission in figure 15. The discrepancy between experiments and model in the discharge current at low currents might be due to the effects of parasitic capacitance in the measurement system.

For the spatio-temporal behaviour of the plasma emission, the model predicts maximum light emission close to the anode surface. However, in the experiments, the maximum is about 1 mm closer to the anode than in the model. The discrepancy in position of the maximum of the light emission might again be due to surface processes on the dielectrics, which were not taken into account in the model.

The voltage across the dielectric barriers was small (<20 V) during the entire voltage cycle. This indicates that the role of the dielectric was very limited in this situation. Charging of the dielectric was not necessary to quench the discharge since the applied voltage dropped during the

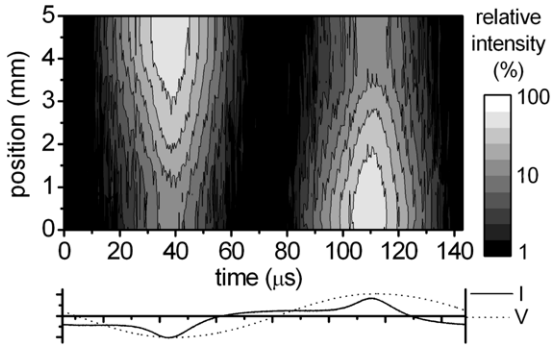

Figure 14. Spatially and temporally resolved measurements of plasma light with a wavelength of 750.4 nm (atomic argon, 4p–4s transition). The dielectric surfaces were located at positions 0 and 5 mm. The measured applied voltage and current are shown under the graph. The voltage of 440 V_{pp} was applied to the lower electrode in the figure.

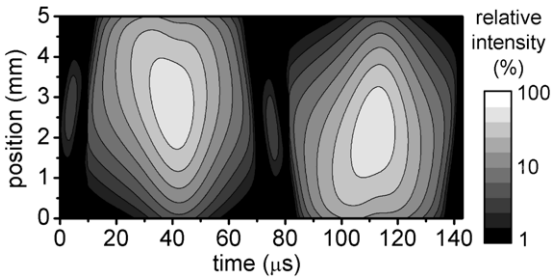

Figure 15. Spatio-temporal development of the calculated rate of reaction $Ar^{**} \rightarrow Ar^{*} + h\nu$ (table 1). This reaction rate can be interpreted as the main part of the total light emission. The dielectric surfaces were located at positions 0 and 5 mm. The voltage was applied to the lower electrode in the figure, which made it the cathode during the first voltage half-cycle and the anode during the second.

discharge, leading to quenching of the discharge. The discharge behaviour is very close to a low-pressure discharge between metal electrodes, driven by a sinusoidal voltage. The breakdown mechanism is still a Townsend breakdown. However, due to the shape of the applied voltage waveform, the electron avalanches do not create enough space-charges to disturb the potential distribution in the discharge gap significantly. Therefore, the transition to a glow-like discharge structure is prevented.

Figure 16 shows several plasma properties calculated by the model for the stable discharge phase ($t = 40\,\mu$s). The general behaviour of the potential and electric field distribution in the gap was similar to the high-voltage (700 V_{pp}) case. Only in the low-voltage (440 V_{pp}) situation, the sheath region was wider and extended to about $x = 2.5$ mm. As a result, the plasma light emission was also positioned further from the cathode surface. However, a significant difference compared with the 700 V_{pp} case in section 4.1 was that the entire plasma is now further from charge-neutrality. In the entire gap, the electron density was more than an order of magnitude smaller than the argon ion density.

In conclusion, when the applied voltage was decreased, the breakdown mechanism of the discharge remained the same, but the discharge structure changed. The buildup of space-charge due to electron avalanches was not large enough to significantly

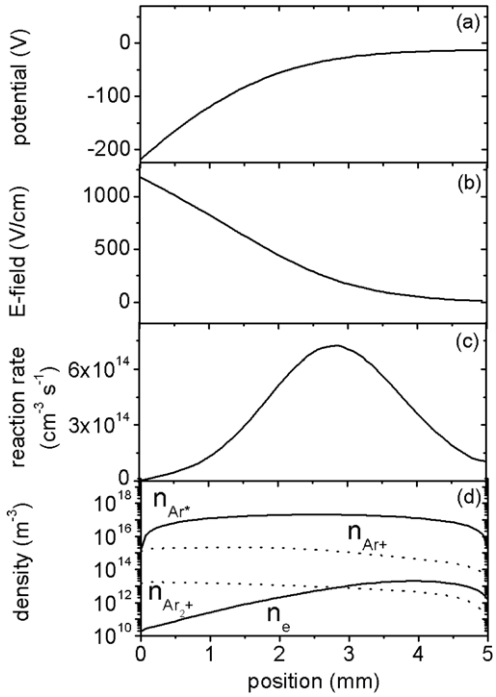

Figure 16. Model calculations of the discharge at $t = 40\,\mu$s. Presented are the distributions in the discharge gap of the potential (*a*), electric field (*b*), $Ar^{**} \rightarrow Ar^{*} + h\nu$ reaction rate (*c*) and charged particle densities (*d*). The cathode is positioned at $x = 0$ and the anode at $x = 5$.

change the potential distribution in the gap. This prevented the discharge from developing into a glow-like structure. Thus the discharge structure at 440 V_{pp} appeared to be more similar to a Townsend discharge.

Furthermore, the influence of the dielectric plates on the discharge behaviour was reduced with decreasing voltage. At the minimum applied voltage (440 V_{pp}), charge buildup at the dielectric barriers did not quench the discharge; this was done by the decrease in the applied voltage waveform.

5. Discussion

5.1. Effects of dielectrics and plasma breakdown

The discharge behaviour of the LPDBD during the breakdown phase can be described by the Townsend breakdown mechanism which was developed to describe the ignition phase of low-pressure discharges between metal, parallel plates [19]. This theory is characterized by multiple electron avalanches driven by the electric field in the gap and secondary electron emission at the cathode due to ion bombardment. The discharge conditions of the LPDBD are considerably different from the standard low-pressure metal electrode discharge. The presence of the insulating, dielectric material covering the electrodes and the sine-shape of the driving voltage change the discharge behaviour. However, during the breakdown phase, the mechanisms driving the ignition process are the same with or without the barriers. Previous investigations on a different discharge system, consisting of a pulsed discharge between parabolic metal electrodes in low-pressure argon gas [35], also concluded that the ignition phase could be described

well by Townsend theory. This indicates that the general concepts of Townsend breakdown are suitable to qualitatively describe breakdown phenomena in a wide range of low-pressure discharges.

The role of the dielectrics during the breakdown phase seems of minor importance, as the breakdown mechanism is qualitatively the same as that between metal electrodes. However, the processes on the dielectric surfaces, for instance electron desorption and photoemission, are not completely understood. These additional processes might have an effect on the discharge behaviour at atmospheric pressure [12,36] but seem to be limited at low pressures.

From more detailed studies, a voltage-controlled transition in the discharge structure could be identified. Our measurements showed that for all applied voltages that were studied the discharge ignited with the same voltage across the discharge gap. However, the development of the breakdown process proceeded differently for different applied voltages. In the case of a high applied voltage (section 4.1), the discharge ignited just after a polarity change in the applied voltage. Here, the charges on the dielectric barrier from the previous discharge caused a residual electric field just below the gap breakdown voltage. Only a small additional, external voltage was needed to start the breakdown process. In this case, the gas voltage was sustained long enough for full discharge development. The electron avalanches during the breakdown phase created enough space-charge to change the electric field distribution in the discharge gap. This resulted in the formation of a glow-like discharge structure.

In the low-voltage case (section 4.2), the barrier voltage was much smaller and the applied voltage had to rise further to cause breakdown. This happened just before the maximum of the sine wave, which means that the voltage was not above the breakdown voltage long enough for full discharge development. The electron avalanches could not produce enough space-charge to distort the local electric field significantly. Therefore, the formation of a glow-like structure was prevented. The discharge was not quenched by the dielectrics but by a reduction of the applied voltage due to the sine-shape.

These measurements showed that in the case of breakdown in DBDs the discharge development depends not only on the voltage amplitude but also on the voltage shape. First of all, the voltage has to be above the breakdown voltage to start the ignition process. Second, the applied voltage has to be sustained long enough for the plasma to build up in multiple electron avalanches and positive space-charges. Additionally, it has to compensate for the opposing electric field generated by particles deposited on the dielectric surfaces.

5.2. Comparison with other discharge types

Our experimental and modelling results showed that during the discharge a stable plasma distribution existed in the gap for several microseconds. The properties of this plasma were in good agreement with the well-known structure of a dc glow discharge between metal electrodes [19]. The LPDBD consisted of a region with high electric field similar to a cathode fall, a glow region with plasma emission resembling a negative glow layer and a dark region in front of the anode. This indicates that our discharge can be interpreted, during the stable regime, as a transient glow-like discharge.

In contrast to the low-pressure discharge, in DBDs in argon at medium and atmospheric pressures a filamentary breakdown and the formation of microdischarges are observed [7]. Under these conditions, regions with high space-charge are generated rapidly, leading to thin discharge channels, as described by the streamer breakdown process. At low pressure, a less localized space-charge region is produced in electron avalanches and the formation of a diffuse plasma is observed. The absence of regions with high, localized space-charge during the breakdown phase, as observed in the LPDBD, is expected to play a role in the formation of diffuse plasmas at atmospheric pressures.

It can be expected that at an intermediate pressure there will be a change from the Townsend breakdown mechanism to the streamer-like breakdown process. It is currently not known how this transition occurs and at which pressures. In order to better understand the discharge, and especially the breakdown phase, measurements of this transition in breakdown mechanism are needed.

6. Summary

We investigated DBDs in low pressure argon gas (LPDBD) by experiments and modelling. The experimental investigations consisted of measurements of the electrical properties and the dynamics of the plasma emission of different spectral lines. In our modelling studies, we used a two-dimensional fluid model to simulate the discharge behaviour of the LPDBD.

We conclude that the breakdown phase of the discharge follows the Townsend breakdown mechanism, similarly to the breakdown phase in low-pressure dc glow discharges between metal electrodes. This in contrast to the breakdown phase in argon DBDs at medium and atmospheric pressures, which have a filamentary breakdown. During the stable discharge phase, the plasma structure shows features which are similar to those of a dc glow discharge.

The effects of the dielectric plates are limited during the breakdown phase. Only in the decay phase do they cause quenching of the discharge. The influence of surface processes, such as electron desorption and photoemission, will be investigated in the future.

At voltages close to the minimum value required to sustain the discharges, the role of the dielectric is of even less importance. The discharge is now quenched by a reduction of the applied voltage due to the sine-shape, instead of quenching by charging the dielectrics.

The presence of argon metastables in the discharge was experimentally monitored through light emission from nitrogen impurities. A metastable density of about $5 \times 10^{17}\ \mathrm{m}^{-3}$ is present during the entire voltage cycle, with only a small ($\sim 10\%$) increase during the discharge. Reactions between these metastable atoms can provide extra initial electrons which can influence the starting of the breakdown process of the discharge. The exact influence of this large and constant density on the behaviour of the discharge needs to be investigated in future research.

Acknowledgments

The authors wish to thank the Centre for Plasma Physics and Radiation Technology in The Netherlands and the Ernst-Moritz-Arndt University of Greifswald in Germany for their support. The experimental work was conducted at the Institute of Physics of the University of Greifswald, supported by DFG-Sonderforschungsbereich 198, 'Kinetics of partially ionized plasmas'.

References

[1] Siemens W 1857 *Poggendorff's Ann. Phys. Chem.* **102** 66–122
[2] Kogelschatz U, Eliasson B and Egli W 1997 *J. Physique IV (France)* **7** C4 47–66
[3] Kogelschatz U 2003 *Plasma Chem. Plasma Process.* **23** 1–46
[4] Wagner H-E, Brandenburg R and Kozlov K V 2004 *J. Adv. Oxid. Technol.* **7** 11–9
[5] Eliasson B and Kogelschatz U 1991 *IEEE Trans. Plasma Sci.* **19** 309–23
[6] Kozlov K V, Wagner H-E, Brandenburg R and Michel P 2001 *J. Phys. D: Appl. Phys.* **34** 3164–76
[7] Merbahi N, Sewraj N, Marchal F, Salamero Y and Millet P 2004 *J. Phys. D: Appl. Phys.* **37** 1664–78
[8] Kanazawa S, Kogoma M, Moriwaki T and Okazaki S 1988 *J. Phys. D: Appl. Phys.* **21** 838–40
[9] Okazaki S, Kogoma M, Uehara M and Kimura Y 1993 *J. Phys. D: Appl. Phys.* **26** 889–92
[10] Gherardi N, Gouda G, Gat E, Ricard A and Massines F 2000 *Plasma Sources Sci. Technol.* **9** 340–6
[11] Massines F, Rabehi A, Decomps P, Ben Gadri R, Ségur P and Mayoux C 1998 *J. Appl. Phys.* **83** 2950–7
[12] Golubovskii Yu B, Maiorov V A, Behnke J and Behnke J F 2002 *J. Phys. D: Appl. Phys.* **35** 751–61
[13] Aldea E, Schrauwen C P G and van de Sanden M C M 2003 *Proc. 16th Int. Symp. on Plasma Chem. ISPC-16, (Taormina, Italy)* CD-ROM file ISPC-521.pdf
[14] Brandenburg R, Maiorov V A, Golubovskii Yu B, Wagner H-E, Behnke J and Behnke J F 2005 *J. Phys. D: Appl. Phys.* **38** 2187–97
[15] Kozlov K V, Brandenburg R, Wagner H-E, Morozov A M and Michel P 2005 *J. Phys. D: Appl. Phys.* **38** 518–29
[16] Navrátil Z, Brandenburg R, Trunec D, Brablec A, St'ahel P, Wagner H-E and Kopecký Z 2006 *Plasma Sources Sci. Technol.* **15** 8–17
[17] Hagelaar G J M, Klein M H, Snijkers R J M M and Kroesen G M W 2001 *J. Appl. Phys.* **89** 2033–9
[18] Brok W J M, van Dijk J, Bowden M D, van der Mullen J J A M and Kroesen G M W 2003 *J. Phys. D: Appl. Phys.* **36** 1967–79
[19] Raizer Y P 1991 *Gas Discharge Physics* (Berlin: Springer)
[20] 1996 *BOLSIG, Boltzmann solver for the SIGLO-series 1* (CPA Toulouse and Kinema Software)
[21] Hagelaar G J M and Kroesen G M W 2000 *J. Comput. Phys.* **159** 1–12
[22] McDaniel E W 1964 *Collision Phenomena in Ionized Gases* (New York: Wiley)
[23] Grigoriev I S and Meilikhov E Z (ed) 1997 *Handbook of Physical Quantities* (Boca Raton, FL: CRC Press)
[24] Ellis H W, Pai R Y, McDaniel E W, Mason E A and Viehland L A 1976 *At. Data Nucl. Data Tables* **17** 177–210
[25] Phelps A V and Petrović Z Lj 1999 *Plasma Sources Sci. Technol.* **8** R21–44
[26] Tachibana K 1986 *Phys. Rev.* A **34** 1007–15
[27] Zapesochnyi P and Shimon L L 1966 *Opt. Spectrosc.* **21** 155–7
[28] McFarland R H and Kinney J D 1965 *Phys. Rev.* **137** A1058–61
[29] Vriens L 1964 *Phys. Lett.* **8** 260–1
[30] Klucharev A N and Vujnović V 1990 *Phys. Rep.* **185** 55–81
[31] Bassett N L and Economou D J 1994 *J. Appl. Phys.* **75** 1931–9
[32] Ashida S, Lee C and Lieberman M A 1995 *J. Vac. Sci. Technol.* A **13** 2498–507
[33] Johnsen R, Chen A and Biondi M A 1980 *J. Chem. Phys.* **73** 1717–20
[34] Mehr F J and Biondi M A 1968 *Phys. Rev.* **176** 322–6
[35] Wagenaars E, Bowden M D and Kroesen G M W 2005 *Plasma Sources Sci. Technol.* **14** 342–50
[36] Golubovskii Yu B, Maiorov V A, Behnke J and Behnke J F 2003 *J. Phys. D: Appl. Phys.* **36** 39–49